First-principles study of topologically protected vortices and ferroelectric domain walls in hexagonal YGaO$_3$

Didrik R. Småbråten [●],[1] Ayako Nakata [●],[2] Dennis Meier [●],[1] Tsuyoshi Miyazaki [●],[2] and Sverre M. Selbach [●][1],[*]

[1]*Department of Materials Science and Engineering, Faculty of Natural Sciences and Technology,*
NTNU Norwegian University of Science and Technology, NO-7491 Trondheim, Norway
[2]*International Center for Materials Nanoarchitectonics (WPI-MANA), National Institute for Materials Science (NIMS),*
1-1 Namiki, Tsukuba, Ibaraki 305-0044, Japan

Ferroelectric behavior on the meso- and macroscopic scale depends on the formation and dynamics of domains and controlling the domain patterns is imperative to device performance. While density functional theory (DFT) calculations have successfully described the basic properties of ferroelectric domain walls, the necessarily small cell sizes used for the calculations hampers DFT studies of complex domain patterns. Here, we simulate large-scale complex ferroelectric domain patterns in ferroelectric YGaO$_3$ using multisite local orbitals as implemented in the DFT code CONQUEST. The multisite local orbital basis set gives similar bulk structural and electronic properties, and atomic domain wall structures and energetics as those obtained with conventional plane-wave DFT. With this basis set model, 3600-atom cells are used to simulate topologically protected vortices. The local atomic structure at the vortex cores is subtly different from the domain walls, with a lower electronic band gap suggesting enhanced local conductance at these cores.

I. INTRODUCTION

Density functional theory (DFT) calculations have shown great success in explaining and predicting material properties [1]. However, because of the poor scaling with number of atoms, the system sizes accessible are typically quite limited. While DFT calculations have been proven to adequately capture most of the bulk properties for relatively small model cells, larger model cells are required for interfaces and surfaces, and more complex geometries, such as surface adsorbed clusters or curved interfaces [2–11].

In the field of ferroelectrics, curved domain walls [12], polar vortices [13–15], and topological defects [16,17] are examples for large-scale geometric features of great fundamental and technological interest. The hexagonal gallates, h-RGaO$_3$ (R = Y, In, Sc, Ho-Lu), are a promising material class for theoretical studies of emergent phenomena in improper ferroelectrics. Many of the results can be generalized and applied for other material classes, such as the isostructural [18] hexagonal manganites, h-RMnO$_3$, which have been intensively studied for their multiferroic properties, domain structure and functional domain walls [16,19,20]. While the domain walls attract attention as possible building blocks for nanoscale electronic components [21–24], the unusual domain pattern [19,25–27] of h-RMnO$_3$ has been studied to address cosmology related questions. Intersections between six domain walls represent topological defects that form following the Kibble-Zurek mechanism [28–30] upon cooling through the ferroelectric Curie temperature ($T_c \approx 1250$ K for YMnO$_3$) [28,31–34].

As compared to their manganite counterparts, the hexagonal gallates have the advantage of being computationally friendly due to the lack of low-temperature magnetism and thus making them a perfect model system for DFT simulations on a large number of atoms. They undergo a qualitatively similar improper ferroelectric phase transition [35,36] from paraelectric $P6_3/mmc$ to ferroelectric $P6_3cm$. The primary order parameter is a so-called nonpolar K_3 mode, which corresponds to a displacement of the R ions along the c axis and a tilt of the GaO$_5$ trigonal bipyramids. As a consequence, a characteristic up-down-down R-corrugation pattern arises as illustrated in Fig. 1(a). The crystal structure consists of alternating layers of R cations and corner-sharing trigonal bipyramids, with two symmetry equivalent R-cation positions (R1 and R2), two apical O (O1 and O2), and two planar O; O3 aligned with R1 and O4 with R2 in the ab plane. Three choices of trimerization centers (O3) [16], combined with two tilt directions for the GaO$_5$ trigonal bipyramids [25,37], give rise to six symmetry equivalent structural domains ($\alpha^\pm$, $\beta^\pm$, and $\gamma^\pm$), each uniquely described by a phase Φ and an amplitude Q of the K_3 mode. The amplitude Q is here quantified by the tilt angle of the apical oxygen relative to the [001] direction, equal to $\sim 5°$ in bulk [31]. The phase Φ is quantified by the tilt direction of the apical oxygen within the ab plane relative to the trimerization center of the α^+ domain [Fig. 1(b)], where Φ of each domain follows the rule $\Phi = n \cdot 60°$ (n is an integer). The R corrugation is strongly coupled to the bipyramidal tilting through the ionic R-O bonds [38], where each structural domain has a unique R-corrugation pattern (up-down-down, up-down-up, etc.). The improper ferroelectric order arises because of a coupling to Φ and Q, given by the relation $P \sim Q^3 \cos 3\Phi$, analogous to the hexagonal manganites [36,37,39]. The ferroelectric domain walls are characterized by a change
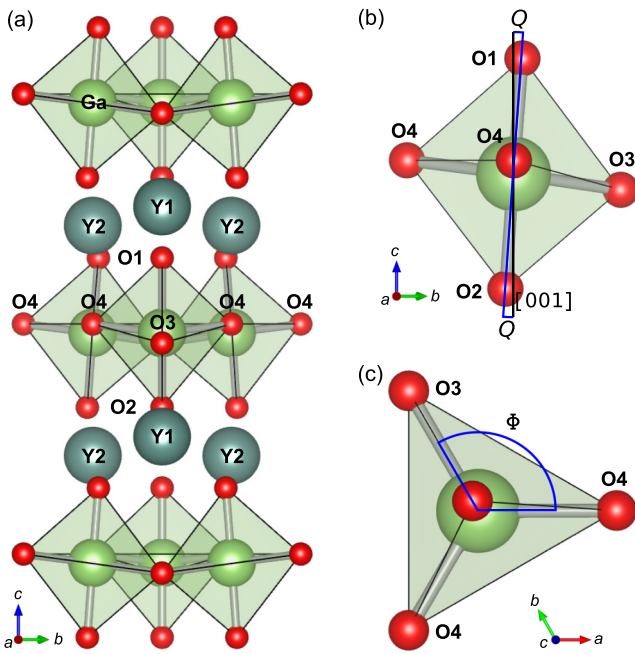
*selbach@ntnu.no

FIG. 1. (a) Crystal structure of hexagonal $YGaO_3$ in the $P6_3cm$ space group, illustrating the Y corrugation, the GaO_5 trigonal bipyramidal tilting, and the symmetry equivalent sites. The amplitude, Q, and phase, Φ, are quantified by (b) the GaO_5 tilt angle relative to the [001] direction and (c) the GaO_5 tilt direction projected onto the ab plane, respectively.

in the phase of $\Delta\Phi = 60°$ across the wall, which corresponds to a change in the sign of the polarization (i.e., the polarization direction) from the coupling to P. The domain walls should, in principle, adopt a nonpolar $P\bar{3}c1$ structure, related to the space group $P6_3cm$ by a rotation of the trigonal bipyramids by 30° in the ab plane with a resulting up-intermediate-down R corrugation, which cancels out the out-of-plane polarization at the center of the wall. The domain wall width is believed to be proportional to the difference in the stability of these two hettotypes, governed by the ionic or covalent nature of the R cation [40,41]. For compounds with more ionic R cations the walls are found to be nearly atomically sharp, on the order of 2–7 Å wide [12,17,41].

While significant progress has been made in DFT studies of materials with the h-RMnO$_3$ structure, including the mechanism of polarization [35], the nature of the improper ferroelectric phase transition [36,38], and the atomic scale structure at the domain walls [12,20–22,37,41–44], detailed atomistic simulations of their topologically protected meeting points [17,45–47] remain elusive. To model such meeting points, a significantly larger number of atoms is required compared to domain wall studies, making traditional DFT computational approaches unfeasible. Here, we study the crystal structure and electronic properties of topological defects and domain walls in improper ferroelectric $YGaO_3$ by large-scale DFT simulations using contracted pseudoatomic orbitals (PAO), as implemented in the highly parallelizable linear-scaling DFT code CONQUEST [2,6,9,48]. We construct a PAO basis set model that gives domain wall structures and energetics similar to conventional plane-wave DFT calcula-

tions. We use this basis set to study domain patterns with 3600 atoms and simulate the sixfold topological defects that arise where domain walls intersect. We find excellent agreement between PAO and plane-wave calculations with respect to the crystal structure, ferroelectric, and electronic properties, as well as the domain wall width, energy, and structure. Our calculations of topologically protected vortices predict that the local crystal structure is only subtly different from the domain wall structure with a small reduction in band gap, suggesting that these cores are more conducting than both bulk and domain walls.

II. METHODOLOGY

We use the first-principles DFT code CONQUEST to treat large-scale $YGaO_3$ supercells. In CONQUEST, real-space local-orbital functions, which are called "support functions", are used to describe the density matrices. The locality of the support functions makes the matrices in the calculations to be sparse, and all the sparse matrix multiplications in CONQUEST are highly parallelized and can be performed in $O(N)$ (where N is the total number of atoms in the system).

The support functions consist of real-space basis functions, where we use computationally efficient PAO functions [49] in the following; PAOs are atomic-orbital-type functions consisting of radial functions (ζ) multiplied with spherical harmonic functions, vanishing at a given cutoff range r_{PAO}. Although the systematic improvement of accuracy is not guaranteed rigorously, the accuracy of PAOs can be improved by (i) increasing the number of the radial functions for each spherical harmonic function, which is called multiple-ζ PAOs, and (ii) including atomic shells of higher angular momentum than the occupied valence shells in the free atom, which is called polarization orbitals.

Since the computational cost scales cubically to the number of the support functions, reducing the number of the support functions is quite important for large-scale calculations. We have recently proposed the multisite support functions (MSSFs) [50], which corresponds to the linear combinations of the PAOs χ of the target atom i and its neighboring atoms k in a multisite cutoff region r_{MS},

$$\phi_{i\alpha}(r) = \sum_{k}^{\text{neighbors}} \sum_{\mu \in k} c_{i\alpha,k\mu} \chi_{k\mu}(r). \quad (1)$$

The multisite support functions are like local molecular-orbital (MO) functions so that we need to consider only the functions corresponding to the occupied local MOs, which enables us to reduce the number of support functions to be minimal-basis size, i.e., single-ζ size.

To determine the linear-combination coefficients $c_{i\alpha,k\mu}$ in Eq. (1), we minimize the total energy with respect to the coefficients [51]. To determine the good initial values of the multisite coefficients, we use the local-filter-diagonalization (LFD) method [50,52,53]. In the LFD method, the multisite coefficients are determined by projecting the local MO coefficients with the cutoff range r_{LFD} on some given localized trial vectors. The LFD method is not rigorously variational because of the projections, but in most cases the method can provide acceptable accuracy even without the subsequent numerical

optimization when r_{MS} is sufficiently large. Therefore, in this study we use only the LFD method to determine the coefficients. The dependence of the accuracy on r_{MS} for the present YGaO$_3$ systems is assessed in Sec. IV A.

In CONQUEST, we have two methods to optimize the electronic density; one is the conventional diagonalization method with $O(N^3)$ scaling and the other is the density matrix minimization method, introducing the cutoff region of the auxiliary density matrix, with $O(N)$ scaling. The $O(N)$ method has a significant advantage regarding the computational costs but requires some additional calculation to obtain the information of bands and MOs [7]. On the other hand, the bands and the MOs are obtained inevitably by the diagonalization method and diagonalization for systems with several thousand atoms by using the MSSFs. Therefore, we use the diagonalization method with the MSSFs in the present study.

III. COMPUTATIONAL DETAILS

A. Basis sets

The PAO basis set calculations in CONQUEST are performed using norm-conserving pseudopotentials constructed by the Troullier-Martins method with Ceperley-Alder flavor and the local density approximation (LDA) functional. Y(4d, 5s), Ga(4s, 4p), and O(2s, 2p) are treated as valence shells, with cutoff radii for the valence shells summarized in Table SI [54]. We investigate three different primitive PAO basis sizes; Single-ζ plus single polarization (SZP), double-ζ plus single polarization (DZP), and triple-ζ plus double polarization (TZDP). The PAOs are prepared by the energy shift method as implemented in Siesta [55,56] with an energy shift of 100 meV for the SZP and DZP PAOs and 50 meV for the TZDP PAOs. The large-scale simulations are performed with contracted PAOs from the primitive TZDP, using the MSSF method described above [50]. The cutoff energy for the charge density grid is set to 100 Ha.

The plane-wave DFT calculations are performed with the projector augmented wave method (PAW) as implemented in VASP [57–59], using the LDA exchange correlation functional with Ceperley-Alder flavor to enable a more direct comparison to that of the PAO basis sets described above. Y (4s, 4p, 4d, 5s), Ga (3d, 4s, 4p), and O (2s, 2p) are treated as valence electrons, with a plane-wave cutoff energy of 550 eV.

B. Geometry optimization

For all geometry optimizations, the atomic positions are relaxed until the forces on all the atoms are below 0.01 eV/Å, with initial lattice parameters set to the fitted V_0 value from the energy-volume curves using the MSSF method with $r_{MS} = r_{LFD} = 12$ Bohr. We use a Monkhorst-Pack grid with a $3 \times 3 \times 3$ k-point density for the 120 atoms $2 \times 2 \times 1$ supercells, a $5 \times 1 \times 3$ k-point density for the 360 and 480 atoms domain pattern supercells, and with a single Γ point in the Brillouin zone for the 3600 atoms supercells. The geometry optimizations with the CONQUEST code are performed using the fast inertial relaxation engine method [5,60], while the geometry optimizations with the VASP code are performed using the conjugate-gradient method.

C. Supercell configurations

We determine the PAO basis set size required for sufficient accuracy by comparing the equilibrium volumes V_0 and bulk moduli B_0 by fitting calculated energy-volume (E-V) curves on 120 atoms $2 \times 2 \times 1$ supercells to the Birch-Murnaghan equation of state [61]. The MSSF method is assessed by calculated E-V curves for contracted PAOs from the primitive TZDP basis set with increasing support function radii $r_{MS} = r_{LFD}$ from 6.0 to 16.0 Bohr. In the following, we denote the value of the support function radii as (r_{MS}-r_{LFD}), where, e.g., $r_{MS} = r_{LFD} = 6.0$ Bohr is denoted (6.0-6.0) and so forth. We assume the experimentally observed c/a ratio for YGaO$_3$ of 1.92 [18] for all volumes.

The local crystal structure and energetics across multiple structural/ferroelectric domain pattern supercells are determined using the primitive TZDP basis set, using the MSSF method contracted from the TZDP basis set and with (r_{MS}-r_{LFD}) of (12.0-12.0), and using plane-wave DFT. We investigate the local crystal structures for the different patterns by the evolution of the order parameter through the phase Φ and tilt Q across the supercells. As model systems, we use 360 atoms $1 \times 12 \times 1$ supercells initialized with (i) a monodomain state to determine the bulk Φ and Q values, (ii) two domains with a change in the phase of $\Delta\Phi = 60°$ (i.e., opposite polarization direction) to model the structure evolution and energetics for isolated domain walls, and (iii) all six domain states in the pattern (α^+, β^-, γ^+, α^-, β^+, γ^-) to model stripe domains with some degree of interface-interface interactions. Because of periodic boundary conditions for the two-domain structures, one domain wall will always be Y1 terminated while the other will be Y2 terminated. For stripe-domain patterns, all domain walls will either be Y1 terminated or Y2 terminated; here, both configurations are investigated. In the following study, motivated by their structural similarity, we assume that YGaO$_3$ adopts the sharp domain wall configuration, which was reported to be lowest in energy for YMnO$_3$ [12]. Note that the 360 atoms $1 \times 12 \times 1$ supercells investigated are in the same order of magnitude as those typically used in the literature [12,20–22,37,41–44]. Hence, we refer to these supercell sizes as "conventional-scale" supercells in the following.

The domain wall formation energies are calculated as

$$E_{DW}^f = \frac{1}{2A}(E_{\uparrow|\downarrow} - E_{\text{mono}}) \quad (2)$$

for the two-domain patterns, and

$$E_{DW}^f = \frac{1}{6A}(E_{\uparrow|\downarrow} - E_{\text{mono}}), \quad (3)$$

for the stripe-domain patterns. Here, $E_{\uparrow|\downarrow}$ is the energy of a two-domain supercell or a stripe-domain pattern supercell, E_{mono} is the energy of a monodomain supercell, and A is the domain wall cross-sectional area. We assume that the different domain walls contribute equally to the total energy of the system.

Next, we structurally relax "large-scale" 3600 atoms $10 \times 12 \times 1$ supercells with two-domain and stripe-domain patterns to determine the robustness of large-scale modeling of
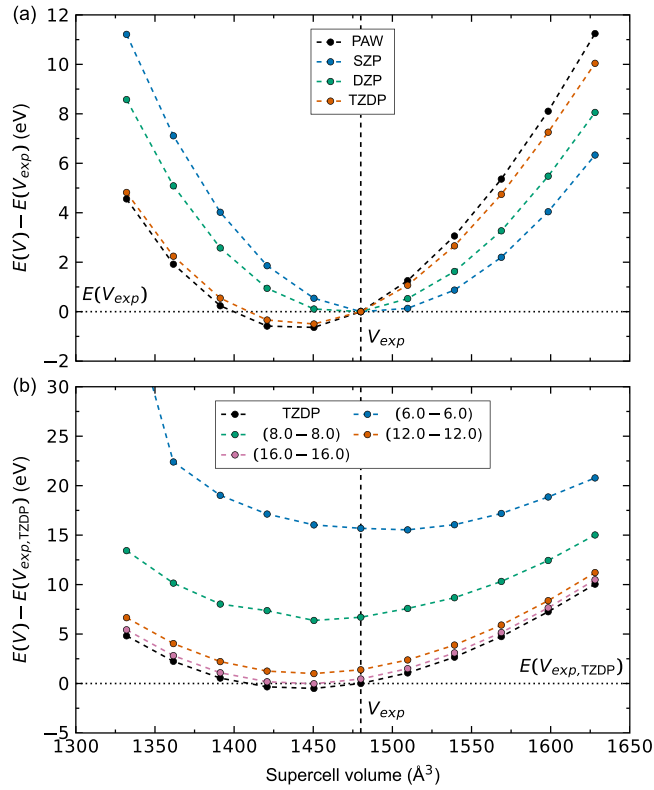
FIG. 2. (a) Calculated energy-volume curves for 120 atoms $2 \times 2 \times 1$ supercells using plane-waves (PAW) and with increasing primitive PAO basis set size from SZP to TZDP. The energies are scaled relative to the energies for each basis set at $V = V_{exp}$. (b) Calculated energy-volume curves for contracted PAOs from the primitive TZDP basis set using the MSSF method, with increasing support function radii (r_{MS}-r_{LFD}). The energies are scaled relative to the energy of the primitive TZDP basis set at $V = V_{exp}$. Note that the large spike at $V = 0.9 V_{exp}$ for (r_{MS}-r_{LFD}) of (6.0-6.0) is not included when fitting the V_0 and B_0 values from the E-V curves.

the improper ferroelectric domain structure in this material class. The resulting evolution in the primary order parameter across the large-scale supercells are compared to those obtained for the similar "conventional-scale" $1 \times 12 \times 1$ supercells. Finally, we investigate the calculated local atomic and electronic structure across a 3600 atoms $10 \times 12 \times 1$ supercell with two vortex/antivortex pairs.

IV. CONVENTIONAL-SCALE DFT CALCULATIONS

A. Assessment of the PAO basis sets

A comparison of the resulting E-V curves for increasing PAO basis set size from SZP to TZDP, and for plane-wave DFT, is shown in Fig. 2(a). The energies at each volume $E(V)$ are scaled relative to the energy obtained using the experimental volume V_{exp} [18] to readily compare the different basis sets. The equilibrium volumes V_0 and bulk moduli B_0 for the different PAO basis set sizes determined from the E-V curves are summarized in Table I. The bulk modulus tends to deviate more from the plane-wave DFT by increasing the PAO basis set size from SZP to TZDP. In contrast, the equilibrium volume tends to converge towards the plane-wave

TABLE I. Fitted bulk modulus B_0 and equilibrium volume V_0 from calculated E-V curves in 120 atoms $2 \times 2 \times 1$ supercells with primitive SZP, DZP, and TZDP PAO basis sets, and with contracted PAOs from the primitive TZDP basis set using the MSSF method with increasing multisite support function radii (r_{MS}-r_{LFD}). Results from plane-wave DFT (PAW) are also included, for comparison. The percent deviation from the primitive TZDP PAOs are shown in parenthesis.

Method	B_0 (GPa)		V_0 (Å^3)	
SZP	181.84	(+3.12)	1488.79	(+3.23)
DZP	181.16	(+2.73)	1470.47	(+1.96)
TZDP	176.34	(0)	1442.23	(0)
MSSF (r_{MS}-r_{LFD})				
(6.0-6.0)	162.71	(−7.73)	1489.70	(+3.29)
(8.0-8.0)	169.44	(−3.91)	1456.70	(+1.00)
(12.0-12.0)	174.64	(−0.96)	1446.95	(+0.33)
(16.0-16.0)	176.62	(+0.16)	1443.59	(+0.09)
PAW	189.66	(+7.55)	1437.63	(−0.32)

results by increasing the PAO basis set size. One of the major disadvantages of PAO basis sets is the lack of systematic convergence with respect to basis set size. In this study, the TZDP basis set is chosen because the equilibrium volume is well described with this basis set size, with a resulting V_0 of 1442.23 Å^3 compared to 1437.63 Å^3 using plane waves. Note that the primitive TZDP basis set renders YGaO$_3$ slightly softer than with the plane waves, with the corresponding bulk moduli of 176.34 and 189.66 GPa, respectively. However, the results from the primitive TZDP PAOs and the plane waves should still give sufficiently similar results in order to compare the two methods directly.

The calculated E-V curves using the MSSF method contracted from the TZDP basis set with increasing multisite support function radii (r_{MS}-r_{LFD}) from (6.0-6.0) to (16.0-16.0) are shown in Fig. 2(b). The energies at each volume $E(V)$ are scaled relative to the energy at $V = V_{exp}$ using the primitive TZDP basis set. First, we notice that by increasing the multisite support function radii (r_{MS}-r_{LFD}), the position of the energy minima converges towards that of the primitive basis. This is also apparent from the fitted V_0 values in Table II, where the V_0 of 1443.59 Å^3 for (r_{MS}-r_{LFD}) of (16.0-16.0) differs only by 0.09% from the V_0 of 1442.23 Å^3 for the primitive TZDP basis set. Secondly, the shape of the E-V curves approaches that of the TZDP basis set, which is also apparent from the fitted B_0 values in Table II. In Table II, an (r_{MS}-r_{LFD})

TABLE II. Comparison of the calculated domain wall widths for two-domain patterns in 360 atoms $1 \times 12 \times 1$ supercells, using plane waves (PAW), with primitive TZDP PAOs, and with contracted PAOs from the primitive TZDP basis set using the MSSF method with (r_{MS}-r_{LFD}) of (12.0-12.0).

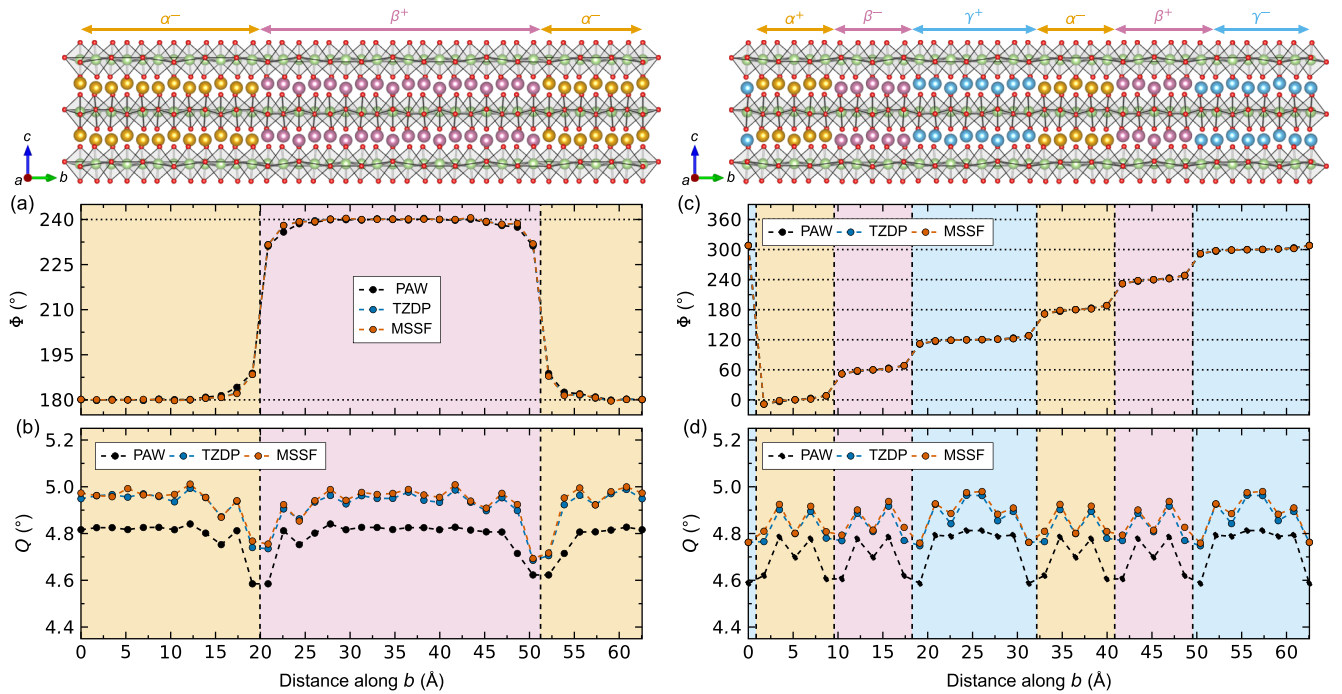| Domain wall	Domain wall width, ξ_6 (Å)		
	PAW	TZDP	MSSF
Y1-terminated	0.72	0.67	0.66
Y2-terminated	0.74	0.69	0.69

FIG. 3. The evolution of the phase Φ and tilt amplitude Q across (a),(b) two-domain patterns and (c),(d) Y2-terminated stripe-domain patterns in 360 atoms $1 \times 12 \times 1$ supercells, using plane-wave DFT (PAW), with primitive TZDP PAOs, and with contracted PAOs from the primitive TZDP basis set using the MSSF method with (r_{MS}-r_{LFD}) of (12.0-12.0).

of (16.0-16.0) results in a B_0 value that differs 0.16% from that of the TZDP calculations. Finally, the absolute value of the energies converges towards the $E(V)$ values for TZDP, which is expected for increasing multisite ranges [50]. From the V_0 and B_0 values in Table II, we assume satisfactory (r_{MS}-r_{LFD}) values of (12.0-12.0), where both the V_0 and the B_0 values of 1446.95 Å^3 and 174.64 GPa are within 1% deviation from the primitive TZDP basis set of 1442.23 Å^3 and 176.34 GPa, respectively. Thus, multisite support radii (r_{MS}-r_{LFD}) of (12.0-12.0) are exclusively used in the following.

We note that irregularities in the shapes of the E-V curves in Fig. 2(b) for (r_{MS}-r_{LFD}) of (6.0-6.0) and (8.0-8.0) are an artefact from the MSSF method: large changes in volume can cause a large change in the number of atoms within the multisite range and, hence, significantly change the calculated total energy [three distinct parabolas can be seen for (r_{MS}-r_{LFD}) of (6.0-6.0) and two distinct parabolas for (r_{MS}-r_{LFD}) of (8.0-8.0)]. These effects can be avoided by applying a smoothing function on the MSSFs [50].

B. Crystal structure and ferroelectric properties

We begin our analysis by determining the ferroelectric polarization of YGaO$_3$ from DFT relaxed 360 atoms $1 \times 12 \times 1$ supercells with an α^- monodomain configuration. All the three basis sets retain the initialized bulk Φ value of 180°. As further demonstrated below, we always retain proper bulk Φ values following the phase rule $\Phi = n \cdot 60°$ in each domain for all domain patterns investigated. Thus, the strong Y1-O3 bonds that govern the GaO$_5$ tilt pattern in the $P6_3cm$ symmetry, i.e., the bulk Φ value in each domain, are well

described with our PAOs. The plane waves give a bulk Q value of 4.85°, while the primitive TZDP basis set and the MSSF method give bulk Q values of 4.96° and 4.98°, respectively, all within ∼3% difference. Since the magnitude of the GaO$_5$ tilt is governed by the strong Y1-O3 bonds, which again governs the improper ferroelectric domain state, the polarization should also be well described by the PAOs. Using a simple point charge model with formal charges, we get a bulk polarization $P = 6.8$ μC/cm^2 using plane waves, while both the primitive TZDP basis set and the MSSF method give a slightly higher bulk polarization of 7.9 μC/cm^2. Note that a simple point charge model using formal charges gives similar bulk polarization as the Berry phase method [41,62].

Next, we address the local structure evolution across the neutral domain walls from DFT relaxed 360 atoms $1 \times 12 \times 1$ supercells with two domains and two domain walls. A comparison of the evolution of the phase Φ and tilt amplitude Q across the domain wall supercells using plane-wave DFT (PAW) or using the PAOs (TZDP and MSSF) is given in Figs. 3(a) and 3(b), respectively. All three methods give comparable Φ profiles as seen in Fig. 3(a). Bulk Φ values are obtained within one unit cell away from the wall center, which indicates nearly atomically sharp domain walls, similar to the case of h-YMnO$_3$ [12]. The Q values close to the walls decrease, Fig. 3(b), where a tendency for a smoother Q evolution across the Y1-terminated walls compared to across the Y2-terminated walls is observed. This is in agreement with our previous work on charged domain walls in YGaO$_3$ [41]. The shapes of the Q profiles are in excellent agreement for all three approaches, with a relative shift of the Q values for the PAOs compared to the plane waves of ∼0.1° in accordance with

the bulk Q values described above. The domain wall widths can be determined by fitting the Φ profiles to the analytical expression [17]

$$\Phi(x) = \Phi_n + \frac{2}{3}\arctan(e^{x/\xi_6}), \tag{4}$$

where Φ_n is the phase in domain n, and ξ_6 is the characteristic length associated with the domain wall, i.e., the domain wall width. The resulting domain wall widths for the Y1-terminated and Y2-terminated walls for the three methods are summarized in Table II. Plane-wave DFT results in an average domain wall width of 0.73 Å, while the primitive TZDP basis set and the MSSF method both give average domain wall widths of 0.68 Å. The PAOs tend to give narrower domain walls than the plane waves, reasoned from the smaller bulk Q and P values in the latter as described above. The differences in domain wall widths are however subtle, on the order of ~0.05 Å. Note that while we observe no trend for the domain wall width with respect to the Y termination from our fits to the Φ profiles, we expect the Y1-terminated walls to be wider than the Y2-terminatied walls analogous to charged domain walls [41]. The difference in width can be attributed to the inherent differences in the local chemical environments at the two walls due to the different Y terminations. This becomes apparent from the Q profiles in Fig. 3(b), where we observe a larger spatial extension of Q values that differ from the bulk around the Y1-terminated wall as compared to the Y2-terminated domain walls, suggesting the first to be wider. The fitted domain wall widths are significantly lower than those

TABLE III. Comparison of the calculated domain wall formation energies in two-domain patterns and stripe-domain patterns in 360 atoms $1 \times 12 \times 1$ and 3600 atoms $10 \times 12 \times 1$ supercells, using plane waves (PAW), with primitive TZDP PAOs, and with contracted PAOs from the primitive TZDP basis set using the MSSF method with (r_{MS}-r_{LFD}) of (12.0-12.0).

Configuration	Domain wall formation energy, E_{DW}^f (mJ/m²)		
	PAW	TZDP	MSSF
Two-domain			
$1 \times 12 \times 1$	13.72	15.22	14.43
$10 \times 12 \times 1$	–	–	14.16
Y1 stripe-domain			
$1 \times 12 \times 1$	13.35	14.76	14.04
Y2 stripe-domain			
$1 \times 12 \times 1$	13.83	15.19	15.21
$10 \times 12 \times 1$	–	–	15.17

observed experimentally (~7 Å [17]), which we attribute to a larger trimerization amplitude, which results in a stronger coupling term to P and, hence, narrower domain walls at 0 K as compared to finite temperatures [31]. Also note that the spatial extensions of the perturbations in Q in Fig. 3(b) indicate domain wall widths on the order of 5–10 Å, as compared to the narrow widths in the order of ~1 Å from the fitted Φ profiles. This is consistent with experimentally reported differences in
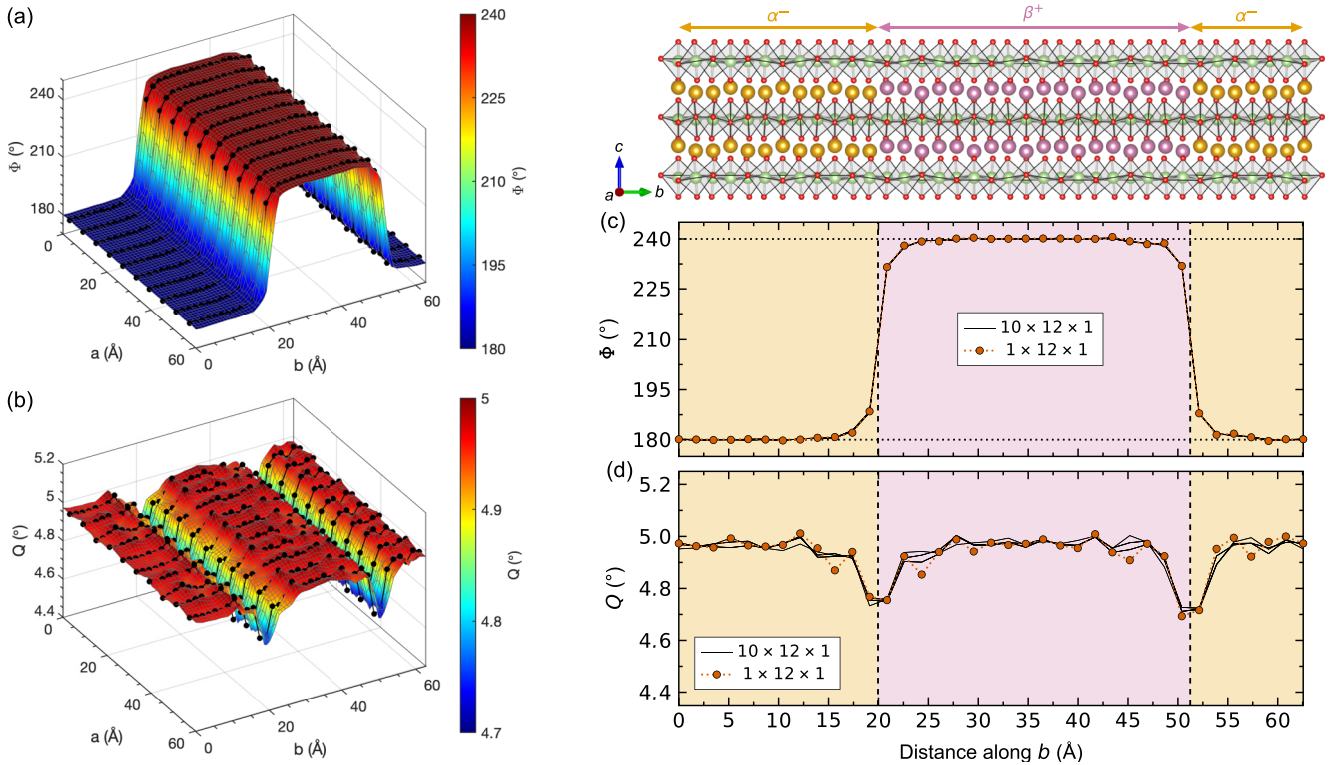

FIG. 4. The evolution of (a) the phase Φ and (b) the tilt amplitude Q in a two-domain pattern 3600 atoms $10 \times 12 \times 1$ supercell. The column averaged Φ and Q profiles for the ten $1 \times 12 \times 1$ supercells constituting the $10 \times 12 \times 1$ supercell are plotted in black circles in (a) and (b), and in black lines in (c) and (d), respectively. The Φ and Q profiles for the $1 \times 12 \times 1$ supercell using the MSSF method [Figs. 3(a) and 3(b)] are plotted in red in (c) and (d), for comparison.
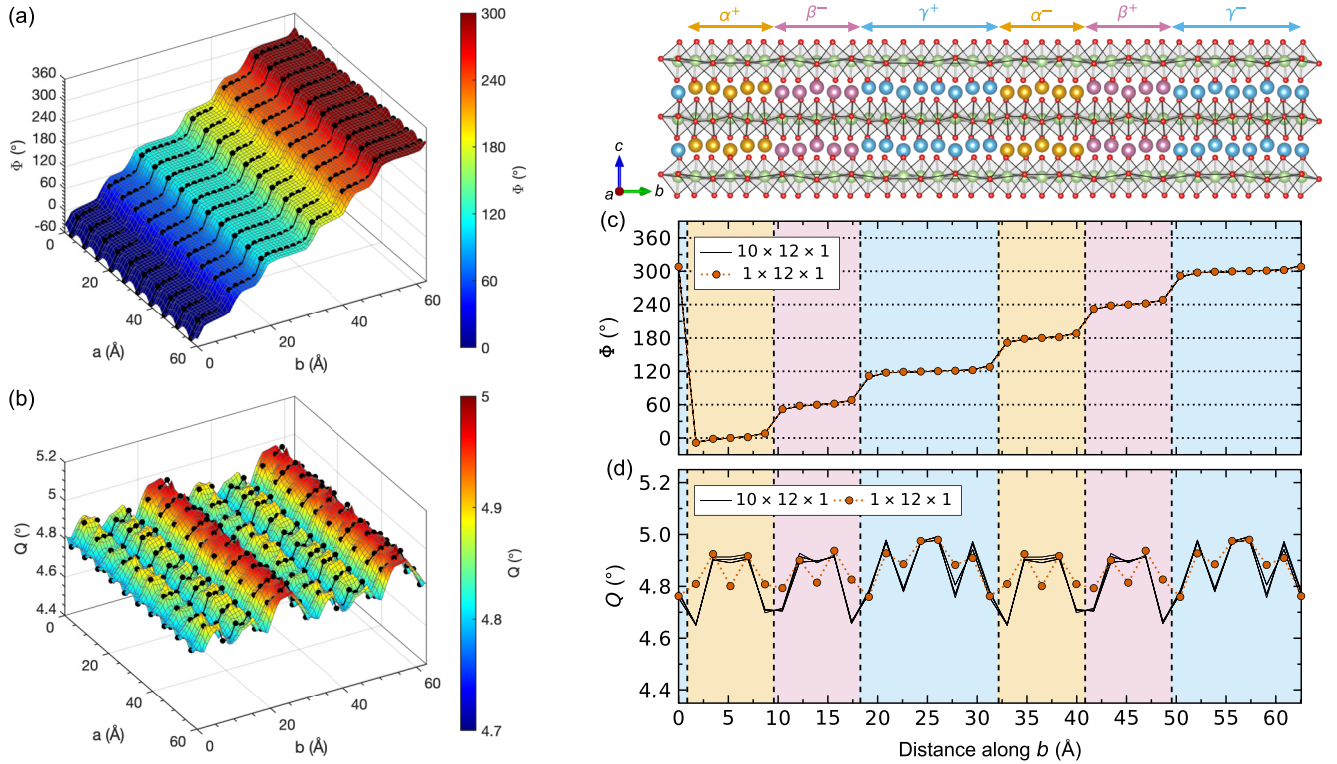
FIG. 5. The evolution of (a) the phase Φ and (b) the tilt amplitude Q in a Y2-terminated stripe-domain pattern 3600 atoms $10 \times 12 \times 1$ supercell. The column averaged Φ and Q profiles for the ten $1 \times 12 \times 1$ supercells constituting the $10 \times 12 \times 1$ supercell are plotted in black circles in (a) and (b), and in black lines in (c) and (d), respectively. The Φ and Q profiles for the $1 \times 12 \times 1$ supercell using the MSSF method [Figs. 3(c) and 3(d)] are plotted in red in (c) and (d), for comparison.

the domain wall widths from fitted Φ or Q profiles, which we attribute to the constant-amplitude approximation included in the analytical expression in Eq. (4) [17].

The resulting domain wall formation energies for the three methods are summarized in Table III. The three approaches give comparable domain wall formation energies of 13.72, 15.22, and 14.43 mJ/m^2 for plane-wave DFT, TZDP PAOs and MSSF PAOs, respectively. All values are within $\sim$3 mJ/m^2 difference ($\sim$0.1 meV/Å^2), which compares to the energy resolution of the DFT calculations.

After determining the ferroelectric structure evolution across isolated neutral domain walls, we next look at domain configurations with significant interface-interface interactions. A comparison of the crystal structure evolution in a Y2-terminated stripe-domain pattern in 360 atoms $1 \times 12 \times 1$ supercell for the three methods is given in Figs. 3(c) and 3(d). In qualitative agreement with the results for the two-domain patterns [Fig. 3(a)], the phase Φ evolves smoothly across the supercells in Fig. 3(c) and bulk values are reproduced at the center of each domain. However, subtle gradients in the Φ profiles occur across each domain, especially apparent in the smaller α and β domains. Such gradients in Φ are consistent with strain fields in the vicinity of the domain walls and interface-interface interactions, which become increasingly significant with decreasing domain wall distance. Conceptually, the results show that the $1 \times 12 \times 1$ supercell is not sufficiently large to avoid interface-interface interactions, which results in small strain fields across the smaller

domains. The interface-interface interactions can be limited by increasing the supercell size, see Figs. S1 and S2 [54] and Supplemental Material Note 1 [54]. The resulting Q profiles in Fig. 3(d) are also comparable to those obtained for the two-domain pattern in Fig. 3(b). The relative shift of $\sim$0.1° is again caused by the inherent difference between the three methods, but the shape of the Q profiles is directly comparable. Similar structure evolutions are observed for the Y1-terminated stripe-domain pattern, see Fig. S2 [54].

The resulting domain wall formation energies for both the Y2-terminated and the Y1-terminated configurations for all three approaches are summarized in Table III and compared to the results obtained from the two-domain patterns. We get domain wall formation energies for the Y2 stripe-domain pattern of 13.83, 15.19, and 15.21 mJ/m^2 using PAW, TZDP, and MSSF, respectively, and 13.35, 14.76, and 14.04 mJ/m^2, respectively, for the Y1 stripe-domain pattern. All values are again within $\sim$3 mJ/m^2 variation.

To summarize, we have shown that the plane-wave DFT and the PAOs give comparable domain wall widths, within $\sim$0.1 Å. The energetics for the two-domain configurations and the stripe-domain configurations are also directly comparable, within 3 mJ/m^2 ($\sim$0.1 meV/Å^2). Hence, we conclude that the improper ferroelectric domain state, with respect to the local crystal structure and the energetics, is well described using our proposed PAO basis set models, which holds even for more complex domain configurations with significant interface-interface interactions.
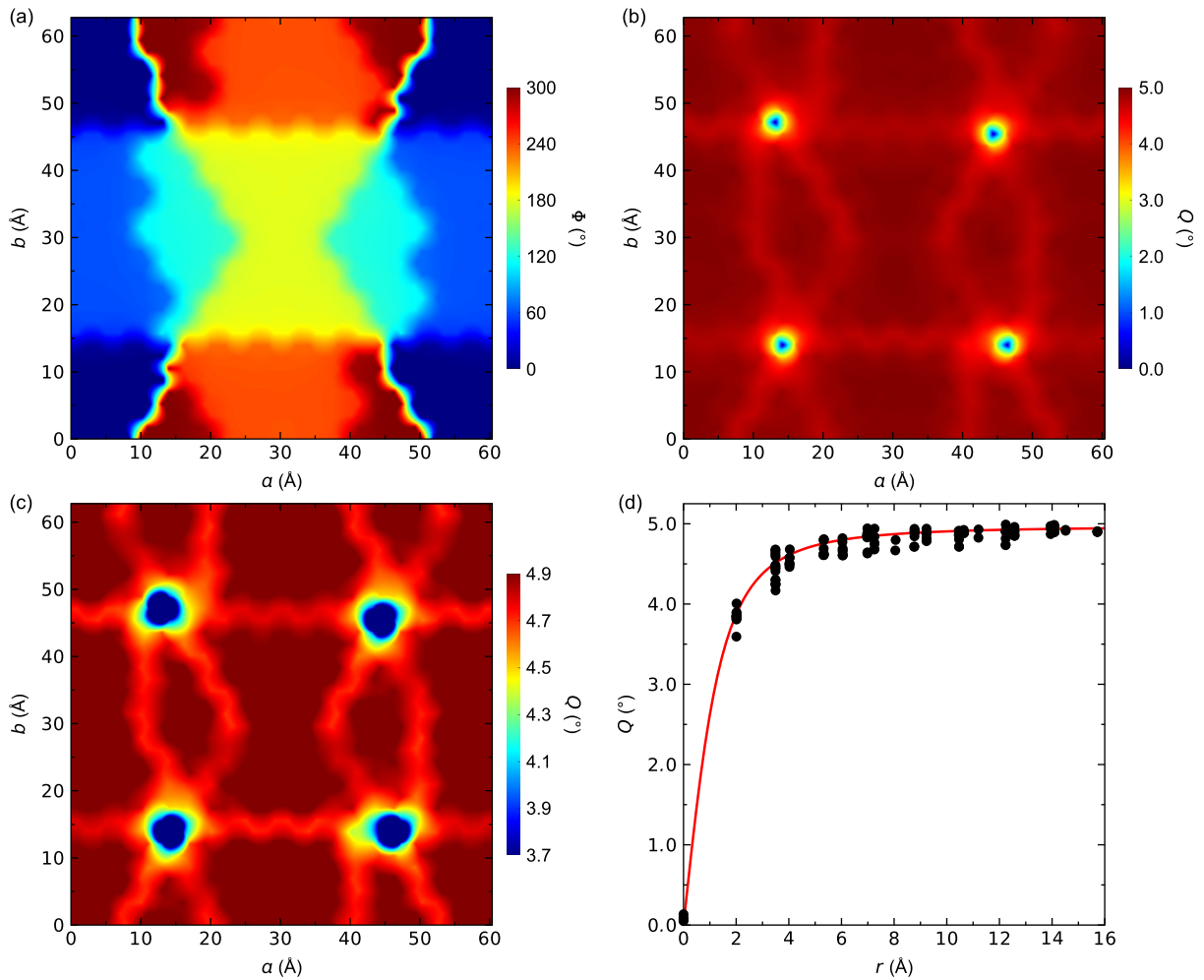
FIG. 6. Surface maps of (a) Φ and (b), (c) Q profiles in a 3600 atoms $10 \times 12 \times 1$ supercell with two vortex/antivortex pairs seen along the crystallographic [001] direction. Each of the colored regions in (a) represents a ferroelectric domain following the phase rule $\Phi = n \cdot 60°$ (n is an integer). The positions of the vortices are indicated by the blue regions in (b). A finer Q surface map is provided in (c), where we clearly see that the vortices are connected by the domain walls (light red/orange color). (d) Plot of the tilt amplitude Q as a function of the distance r from the vortex core. The black dots correspond to the calculated values, and the solid red line is the analytical expression $Q(r) = Q_0 \frac{r/\xi}{\sqrt{2 + (r/\xi)^2}}$ with the fitted core size $\xi = 1.14$ Å.

V. LARGE-SCALE DFT CALCULATIONS

We have now established that our PAO basis set model gives a sufficiently accurate description of the improper ferroelectric domain state. In the following, we will focus on large-scale DFT simulations on 3600 atoms $10 \times 12 \times 1$ supercells with increasing complexity of the domain pattern, using the MSSF method.

A. Ferroelectric domain walls

First, we investigate large-scale simulations of the two-domain pattern described above. The calculated Φ and Q profiles across a 3600 atoms $10 \times 12 \times 1$ supercell with a two-domain configuration are given in Figs. 4(a) and 4(b), respectively. The resulting evolution of Φ [Fig. 4(a)] resembles that obtained for the 360 atoms $1 \times 12 \times 1$ supercell in

Fig. 3(a), where a smooth evolution in Φ is observed with nearly atomically sharp walls. Similarly, we observe abrupt changes in Q across the walls [Fig. 4(b)], with reduced Q values near the domain wall centers. To further elaborate this, we have extracted the layer-averaged Φ and Q profiles for the ten 360 atoms $1 \times 12 \times 1$ supercells constituting the 3600 atoms supercell, plotted in black lines in Figs. 4(c) and 4(d), respectively. The profiles from the 360 atoms $1 \times 12 \times 1$ supercell in Figs. 3(a) and 3(b) using the MSSF method are also plotted in red circles, for comparison. As becomes apparent, there are no significant differences in the structural evolution for the two supercell sizes. Only at the quantitative level, there are some subtle discrepancies in the Q profiles in the order of 0.1°. The resulting domain wall formation energies are given in Table III, where the 3600 atoms supercell has an E_{DW}^f of 14.83 mJ/m^2 compared to 14.43 mJ/m^2 for the 360 atoms supercell.

B. Stripe-domain patterns

Next, we turn to large-scale simulations of stripe-domain patterns. As a proof of concept, only the Y2-terminated configuration will be investigated. The calculated Φ and Q profiles across a 3600 atoms $10 \times 12 \times 1$ supercell with an Y2-terminated stripe-domain configuration, similar to the one described above, are given in Figs. 5(a) and 5(b), respectively. The phase Φ follows the anticlockwise pattern α^+ to γ^-, as shown by the resulting smooth evolution in Φ across the supercell in Fig. 5(a), comparable to the results for the 360 atoms supercell [Fig. 3(c)]. The evolution in Q in Fig. 5(b) is also similar to that observed for the 360 atoms super-cell [Fig. 3(d)], where the Q values are reduced near the domain wall center. The planar averaged Φ and Q profiles for the ten constituting $1 \times 12 \times 1$ supercells are plotted as black lines in Figs. 5(c) and 5(d), respectively. The results obtained for the 360 atoms $1 \times 12 \times 1$ supercell in Figs. 3(c) and 3(d) using the MSSF method are plotted in red circles, for comparison. As for the 3600 atoms two-domain pattern supercell in Fig. 4, no significant qualitative differences for the two supercell sizes are observed. The Q profiles show small quantitative deviations within $\sim 0.2°$. The domain wall formation energies (Table III) are also comparable, with E_{DW}^f of 14.91 and 15.21 mJ/m^2 for the 3600 atoms supercell and 360 atoms supercell, respectively. In summary, the results in Fig. 5 demonstrate that our large-scale DFT model is applicable to narrow ferroelectric domains and, hence, robust against significant interface-interface interactions.

C. Topologically protected vortices

The robustness of the large-scale DFT model is crucial for the investigation of the topologically protected meeting points of domain walls in YGaO$_3$, leading to the formation of atomic-scale vortex structures. Our model system is a $10 \times 12 \times 1$ supercell consisting of two vortex/antivortex pairs, where the domain walls and the vortices are initialized in the high-symmetry $P6_3/mmc$ structure (see Fig. S3 [54]). The geometry-optimized Φ and Q profiles are given in Figs. 6(a) and 6(b), respectively. The domain walls can be traced by the abrupt changes in the phase Φ in (a) and by the reduced Q values in (b). The position of the domain walls becomes even clearer by zooming in into the Q range in (c), where the "lit up" light red/orange features correspond to the domain walls. The tilt angle Q is observed to be abruptly reduced to $\sim 0.1°$ at the four vortex/antivortex cores. This becomes apparent from the plot of the tilt angle Q as a function of the distance r from the vortex core in Fig. 6(d), where we have extracted the Q profiles along b for the two constituting 360 atoms $1 \times 12 \times 1$ supercells containing the cores. To quantify the spatial extension of the cores, we fit the $Q(r)$ profile in Fig. 6(d) to the analytical expression $Q(r) \approx \frac{r/\xi}{\sqrt{2 + (r/\xi)^2}} Q_0$ [17], where ξ is the size of the core and Q_0 is the bulk amplitude. The resulting core size is 1.14 Å, which— similar to the calculated domain wall width— is smaller than the experimental value. Again, we attribute this to a larger trimerization amplitude at 0 K as compared to finite temperatures.

Looking closely at the crystal structure in the vicinity of the vortices as shown in Figs. 7(a) and 7(b), the drop in Q is observed for one GaO$_5$ trigonal bipyramid only, while the
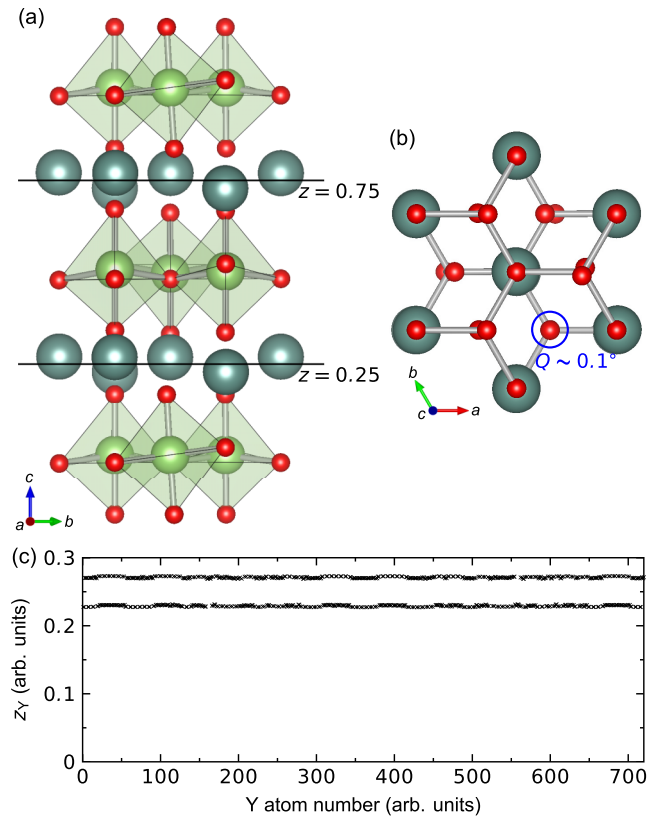

FIG. 7. (a),(b) Representative crystal structure at a topological defect vortex viewed along a and c, respectively. The horizontal lines in (a) correspond to the high-symmetric Y positions in the $P6_3/mmc$ structure. The Ga ions are hidden in (b), to more clearly visualize the resulting GaO$_5$ tilt pattern. The oxygen marked by the blue circle in (b) corresponds to a tilt of $Q \sim 0.1°$. (c) Relaxed z component for all the Y in the 3600 atoms supercell, where all values are shifted to the corresponding $0.25 \pm \Delta z$ values.

surrounding GaO$_5$ polyhedra in the first coordination shell have values of $\sim 3.8°$, close to that at the center of the domain walls. In addition, none of the Y cations is located at its high-symmetry position as shown in Fig. 7(c). This indicates that the vortices adopt $P3c1$ symmetry, which is a subgroup of the space groups $P6_3cm$ and $P\bar{3}c1$ observed in the domains and at the domain wall centers, respectively (i.e., the averaged symmetry of all six domains). The latter is consistent with recent local structure investigations of the ferroelectric phase transition in YMnO$_3$, where it was found that the local structure does not adopt the $P6_3/mmc$ aristotype structure inferred from conventional diffraction, but rather adopts a range of structures with $P3c1$ symmetry [38].

Since the charge density is also calculated in our large-scale DFT simulations, this opens the possibility for probing changes in the electronic properties across the large-scale domain patterns, including the behavior at the vortex/antivortex structures. Such investigations are not available with other large-scale atomistic modeling approaches such as molecular-dynamics or Monte Carlo simulations. The total electronic density of states (DOS) for the vortex/antivortex supercell in YGaO$_3$ is shown in Fig. 8(a), with a calculated electronic band gap of 3.20 eV comparable to the one for a corresponding
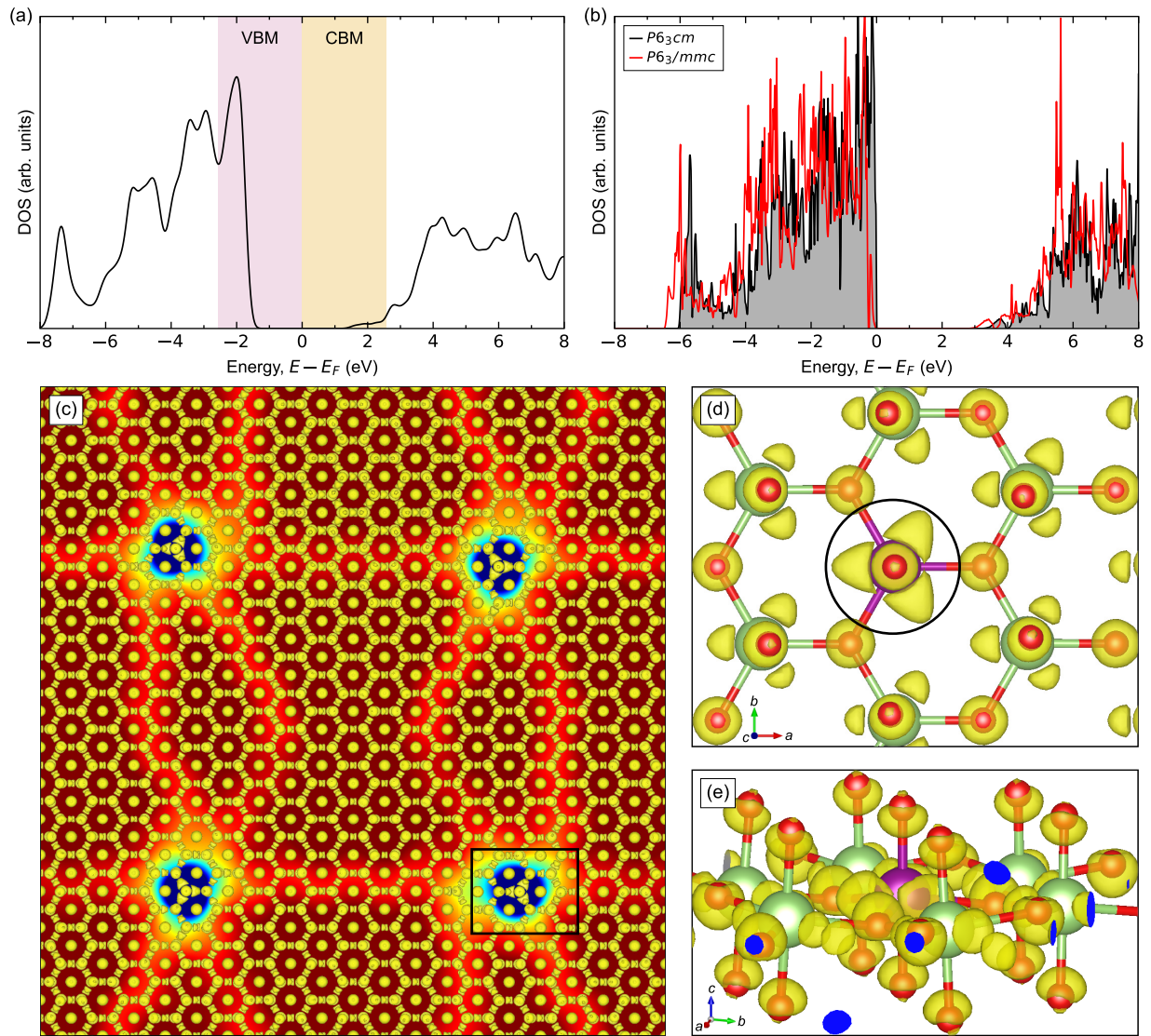
FIG. 8. (a) Total electronic DOS for the 3600 atoms $10 \times 12 \times 1$ vortex/antivortex supercell. (b) Comparison of the DOS for $YGaO_3$ unit cells with tilted GaO_5 trigonal bipyramids ($P6_3cm$), and by rectifying the GaO_5 polyhedra ($P6_3/mmc$). (c) Partial charge density of the bottom of the conduction band (CBM) across the supercell, imposed on top of the Q profile from Fig. 6(c). (d),(e) Detailed features of the charge density of the CBM surrounding the vortex core marked in black in (c), only showing the Ga layer with the rectified GaO_5 (marked in purple). The pronounced nonbonding CBM charge at the vortex core is marked by the black circle in (d).

large-scale monodomain supercell of 3.22 eV. To elaborate this, we have calculated the partial charge density of the top of the valence band (VBM) and the bottom of the conduction band (CBM) indicated by the shaded areas in the total DOS in Fig. 8(a). The CBM partial charge is visualized in Fig. 8(c), imposed on top of the Q profile in Fig. 6(c). The CBM charge density is more pronounced at the GaO_5 trigonal pyramid at the vortex core centers compared to the bulk. The shape of the charge density is similar to that of in-plane Ga $4s$ and O $2p$ nonbonding states, which govern the conduction band minimum in bulk $YGaO_3$ (Fig. S4 [54]). This becomes apparent from the detailed features of the CBM surrounding the vortex core in Figs. 8(d) and 8(e), emphasized by the black circle in Fig. 8(d). While these changes are subtle, they indicate a reduction in the band gap at the vortex cores. We observe no correlation between the CBM and the domain walls. This is

in agreement with the electronic properties for neutral domain walls [12] and can be attributed to a subtle change in the amplitude Q at the domain walls, as compared to the significant reduction in Q at the vortices. No changes in the VBM are observed (Fig. S5 [54]).

The changes in the electronic properties at the vortices can be reasoned from the aforementioned changes in the local crystal structure across the vortex supercell. At the vortex core, the rectification of the GaO_5 trigonal bipyramids gives a reduction in the band gap. To exemplify this, we have calculated the DOS for $YGaO_3$ unit cells in the low-symmetry $P6_3cm$ phase and for a unit cell with rectified GaO_5 trigonal bipyramids, i.e., high-symmetric $P6_3/mmc$, using the plane-wave basis set, Fig. 8(b). The comparison in Fig. 8(b) shows a decrease in the band gap from 3.19 to 2.76 eV, which confirms that the band gap will be reduced at, or in the vicinity of, the

vortex cores, caused by the rectification of the GaO_5 trigonal bipyramids.

VI. DISCUSSION AND CONCLUSION

In this study, we confirm that PAOs are well suited for describing ferroelectrics by carefully constructing and testing the accuracy of the basis set. The large-scale DFT calculations are performed by calculating the full Hamiltonian, with a resulting $O(N^3)$ scaling with N number of atoms in the system. By using the efficient multisite support function method as implemented in the highly parallelizable DFT code CONQUEST, even with this poor $O(N^3)$ scaling we are able to calculate complex system sizes exceeding 3000+ atoms with sufficient accuracy and within a reasonable time frame. Using the multisite support functions and the $O(N)$ method together will enable further investigations of large insulating systems in the future.

Improper ferroelectric domain walls in the hexagonal manganites have been extensively studied both experimentally [16,17,19–24,63–67] and by DFT simulations [12,20–22,37,41–44], whereas for the hexagonal gallates (h-RGaO$_3$) only the charged domain walls have been assessed using DFT [41]. Concerning neutral domain walls, our calculations reveal that their atomic structures are directly comparable to YMnO$_3$ [12], as the wall formation is governed by the ionic nature of the Y-O bonds, and not the Mn-O or Ga-O bonds [38,40]. As a consequence, the domain wall energetics are of the same order of magnitude, too, here reported to be ∼13–15 mJ/m^2 compared to ∼11 mJ/m^2 in YMnO$_3$ [12]. Hence, our calculated domain patterns in h-RGaO$_3$ are expected to be directly comparable to the ones observed in h-RMnO$_3$, reasoned from their similar ionic R-O bonding. Furthermore, our results reveal a universal trend showing that R-O bonds govern the domain wall structure independent of the charge state [41], which is consistent with the improper ferroelectricity.

The similarity of the two systems becomes apparent by comparing the domain patterns calculated for in h-RGaO$_3$ to scanning transmission electron microscopy studies on h-RMnO$_3$ [17,45–47]. The changes in R corrugation across the neutral domain walls are in good qualitative agreement with the atomically resolved studies. We find that the phase Φ smoothly evolves across the walls and the amplitude Q decreases close to walls, consistent with the experimentally resolved profiles [17]. We note that the Φ and Q profiles in Ref. [17] are extracted from the R-cation displacements from the $P6_3/mmc$ paraelectric phase. These profiles are expected to be directly comparable to those extracted from to the GaO_5 tilting (this work), as demonstrated above, since R corrugation and GaO_5 tilting are strongly coupled through the ionic R-O bonds.

The recent implementation of spin-polarized multisite calculations in CONQUEST [68] allows for large-scale DFT calculations on magnetic systems, such as, e.g., multiferroics, which is of high technological interest. The results here can be generalized and applied to other ferroelectric, multiferroic, and dielectric material systems, which should provide a solid foundation for explaining the fundamental physics of emer-gent topological phenomena and new states of matter at the atomic scale.

An alternate strategy to model different domain wall profiles is to use a phase field approach [69] combined with Ginzburg-Landau-Devonshire potentials parameterized using DFT [70,71]. Such phenomenological modeling approaches have been demonstrated to successfully describe charged domain walls in YGaO$_3$ [41], as well as topological defects in the hexagonal manganites [37,72]. While we see clear similarities between our results from large-scale DFT calculations using CONQUEST and results from phenomenological modeling, we note, however, that phenomenological modeling approaches cannot capture some of the subtle local perturbations on the atomic scale, such as the asymmetric domain wall crystal structure with respect to Y termination [41], that we can extract from our large-scale atomistic DFT simulations. Thus, we are confident that large-scale DFT calculations using CONQUEST can provide a significant contribution within multiscale research approaches in the near future.

In summary, we have constructed a contracted PAO basis set model for improper ferroelectric hexagonal YGaO$_3$ suitable for efficient large-scale DFT simulations. The PAOs give bulk equilibrium volumes and bulk moduli within 5% deviation from the results obtained using conventional plane-wave DFT, depending on the basis set size and multisite support function radii. The improper ferroelectric domain state is well described by the PAOs, with bulk ferroelectric properties and atomic-scale domain wall structures and energetics comparable to plane-wave DFT, even for large-scale systems consisting of 3600 atoms. We also demonstrate the robustness of our PAO basis set model by relaxing a complex domain pattern supercell consisting of two trimerization vortex/antivortex pairs. The crystal structure of the vortex/antivortex pair cores is found to differ only slightly from the domain wall structure, described by a subgroup ($P3c1$) of the space groups that describe the domain and domain wall states ($P6_3cm$ and $P\bar{3}c1$) in YGaO$_3$. A local subtle reduction of the electronic band gap is calculated at the cores, predicting enhanced conductivity at trimerization vortices in YGaO$_3$, exceeding the conductivity of the bulk and the individual neutral domain walls that meet at its core.

[1] K. Lejaeghere, G. Bihlmayer, T. Björkman, P. Blaha, S. Blügel, V. Blum, D. Caliste, I. E. Castelli, S. J. Clark, A. Dal Corso *et al.*, Science **351**, aad3000 (2016).

[2] D. R. Bowler, R. Choudhury, M. J. Gillan, and T. Miyazaki, Phys. Status Solidi **243**, 989 (2006).

[3] T. Miyazaki, D. R. Bowler, R. Choudhury, and M. J. Gillan, Phys. Rev. B **76**, 115327 (2007).

[4] T. Miyazaki, D. R. Bowler, M. J. Gillan, and T. Ohno, J. Phys. Soc. Jpn. **77**, 123706 (2008).

[5] M. Arita, S. Arapan, D. R. Bowler, and T. Miyazaki, J. Adv. Simul. Sci. Eng. **1**, 87 (2014).

[6] D. R. Bowler and T. Miyazaki, J. Phys.: Condens. Matter **22**, 074207 (2010).

[7] A. Nakata, Y. Futamura, T. Sakurai, D. R. Bowler, and T. Miyazaki, J. Chem. Theory Comput. **13**, 4146 (2017).

[8] C. O'Rourke, S. Y. Mujahed, C. Kumarasinghe, T. Miyazaki, and D. R. Bowler, J. Phys.: Condens. Matter **30**, 465303 (2018).

[9] A. Nakata, J. Baker, S. Mujahed, J. T. L. Poulton, S. Arapan, J. Lin, Z. Raza, S. Yadav, L. Truflandier, T. Miyazaki, and D. R. Bowler, J. Chem. Phys. **152**, 164112 (2020).

[10] C. Romero-Muñiz, A. Nakata, P. Pou, D. R. Bowler, T. Miyazaki, and R. Pérez, J. Phys.: Condens. Matter **30**, 505901 (2018).

[11] T. Miyazaki, ECS Trans. **86**, 269 (2018).

[12] Y. Kumagai and N. A. Spaldin, Nat. Commun. **4**, 1540 (2013).

[13] A. K. Yadav, C. T. Nelson, S. L. Hsu, Z. Hong, J. D. Clarkson, C. M. Schlepuëtz, A. R. Damodaran, P. Shafer, E. Arenholz, L. R. Dedon, D. Chen, A. Vishwanath, A. M. Minor, L. Q. Chen, J. F. Scott, L. W. Martin, and R. Ramesh, Nature (London) **530**, 198 (2016).

[14] Z. Hong, A. R. Damodaran, F. Xue, S. L. Hsu, J. Britson, A. K. Yadav, C. T. Nelson, J. J. Wang, J. F. Scott, L. W. Martin, R. Ramesh, and L. Q. Chen, Nano Lett. **17**, 2246 (2017).

[15] S. L. Hsu, M. R. McCarter, C. Dai, Z. Hong, L. Q. Chen, C. T. Nelson, L. W. Martin, and R. Ramesh, Adv. Mater. **31**, 1901014 (2019).

[16] T. Choi, Y. Horibe, H. T. Yi, Y. J. Choi, W. Wu, and S. W. Cheong, Nat. Mater. **9**, 253 (2010).

[17] M. E. Holtz, K. Shapovalov, J. A. Mundy, C. S. Chang, Z. Yan, E. Bourret, D. A. Muller, D. Meier, and A. Cano, Nano Lett. **17**, 5883 (2017).

[18] S. Geller, J. B. Jeffries, and P. J. Curlander, Acta Crystallogr. Sect. B **31**, 2770 (2002).

[19] M. Fiebig, T. Lottermoser, D. Fröhlich, A. V. Goltsev, and R. V. Pisarev, Nature (London) **419**, 818 (2002).

[20] D. Meier, J. Seidel, A. Cano, K. Delaney, Y. Kumagai, M. Mostovoy, N. A. Spaldin, R. Ramesh, and M. Fiebig, Nat. Mater. **11**, 284 (2012).

[21] J. A. Mundy, J. Schaab, Y. Kumagai, A. Cano, M. Stengel, I. P. Krug, D. M. Gottlob, H. Doğanay, M. E. Holtz, R. Held, Z. Yan, E. Bourret, C. M. Schneider, D. G. Schlom, D. A. Muller, R. Ramesh, N. A. Spaldin, and D. Meier, Nat. Mater. **16**, 622 (2017).

[22] J. Schaab, S. H. Skjærvø, S. Krohns, X. Dai, M. E. Holtz, A. Cano, M. Lilienblum, Z. Yan, E. Bourret, D. A. Muller, M. Fiebig, S. M. Selbach, and D. Meier, Nat. Nanotechnol. **13**, 1028 (2018).

[23] M. P. Campbell, J. P. V. McConville, R. G. P. McQuaid, D. Prabhakaran, A. Kumar, and J. M. Gregg, Nat. Commun. **7**, 13764 (2016).

[24] W. Wu, Y. Horibe, N. Lee, S. W. Cheong, and J. R. Guest, Phys. Rev. Lett. **108**, 077203 (2012).

[25] T. Jungk, Á. Hoffmann, M. Fiebig, and E. Soergel, Appl. Phys. Lett. **97**, 012904 (2010).

[26] M. Lilienblum, E. Soergel, and M. Fiebig, J. Appl. Phys. **110**, 052007 (2011).

[27] E. Hassanpour, V. Wegmayr, J. Schaab, Z. Yan, E. Bourret, T. Lottermoser, M. Fiebig, and D. Meier, New J. Phys. **18**, 043015 (2016).

[28] S. M. Griffin and N. A. Spaldin, J. Phys.: Condens. Matter **29**, 343001 (2017).

[29] S. Z. Lin, X. Wang, Y. Kamiya, G. W. Chern, F. Fan, D. Fan, B. Casas, Y. Liu, V. Kiryukhin, W. H. Zurek, C. D. Batista, and S. W. Cheong, Nat. Phys. **10**, 970 (2014).

[30] S. C. Chae, N. Lee, Y. Horibe, M. Tanimura, S. Mori, B. Gao, S. Carr, and S. W. Cheong, Phys. Rev. Lett. **108**, 167603 (2012).

[31] A. S. Gibbs, K. S. Knight, and P. Lightfoot, Phys. Rev. B **83**, 094111 (2011).

[32] M. Lilienblum, T. Lottermoser, S. Manz, S. M. Selbach, A. Cano, and M. Fiebig, Nat. Phys. **11**, 1070 (2015).

[33] S. M. Griffin, M. Lilienblum, K. T. Delaney, Y. Kumagai, M. Fiebig, and N. A. Spaldin, Phys. Rev. X **2**, 041022 (2012).

[34] Q. N. Meier, M. Lilienblum, S. M. Griffin, K. Conder, E. Pomjakushina, Z. Yan, E. Bourret, D. Meier, F. Lichtenberg, E. K. H. Salje, N. A. Spaldin, M. Fiebig, and A. Cano, Phys. Rev. X **7**, 041014 (2017).

[35] B. B. Van Aken, T. T. M. Palstra, A. Filippetti, and N. A. Spaldin, Nat. Mater. **3**, 164 (2004).

[36] C. J. Fennie and K. M. Rabe, Phys. Rev. B **72**, 100103 (2005).

[37] S. Artyukhin, K. T. Delaney, N. A. Spaldin, and M. Mostovoy, Nat. Mater. **13**, 42 (2014).

[38] S. H. Skjærvø, Q. N. Meier, M. Feygenson, N. A. Spaldin, S. J. L. Billinge, E. S. Bozin, and S. M. Selbach, Phys. Rev. X **9**, 031001 (2019).

[39] A. Cano, Phys. Rev. B **89**, 214107 (2014).

[40] Y. Kumagai, A. A. Belik, M. Lilienblum, N. Leo, M. Fiebig, and N. A. Spaldin, Phys. Rev. B **85**, 174422 (2012).

[41] D. R. Småbråten, Q. N. Meier, S. H. Skjærvø, K. Inzani, D. Meier, and S. M. Selbach, Phys. Rev. Mater. **2**, 114405 (2018).

[42] S. H. Skjærvø, D. R. Småbråten, N. A. Spaldin, T. Tybell, and S. M. Selbach, Phys. Rev. B **98**, 184102 (2018).

[43] P. Barrozo, D. R. Småbråten, Y. Tang, B. Prasad, S. Saremi, R. Ozgur, V. Thakare, R. A. Steinhardt, M. E. Holtz, V. A. Stoica, L. W. Martin, D. G. Schlom, S. M. Selbach, and R. Ramesh, Adv. Mater. **32**, 2000508 (2020).

[44] X. Wu, U. Petralanda, L. Zheng, Y. Ren, R. Hu, S. W. Cheong, S. Artyukhin, and K. Lai, Sci. Adv. **3**, e1602371 (2017).

[45] Q. H. Zhang, L. J. Wang, X. K. Wei, R. C. Yu, L. Gu, A. Hirata, M. W. Chen, C. Q. Jin, Y. Yao, Y. G. Wang, and X. F. Duan, Phys. Rev. B **85**, 020102 (2012).

[46] Q. Zhang, G. Tan, L. Gu, Y. Yao, C. Jin, Y. Wang, X. Duan, and R. Yu, Sci. Rep. **3**, 2741 (2013).

[47] J. Li, F.-K. Chiang, Z. Chen, C. Ma, M.-W. Chu, C.-H. Chen, H. Tian, H. Yang, and J. Li, Sci. Rep. **6**, 28047 (2016).

[48] E. Hernández, M. Gillan, and C. Goringe, Phys. Rev. B **53**, 7147 (1996).

[49] D. R. Bowler, J. S. Baker, J. T. L. Poulton, S. Y. Mujahed, J. Lin, S. Yadav, Z. Raza, and T. Miyazaki, Jpn. J. Appl. Phys. **58**, 100503 (2019).

[50] A. Nakata, D. R. Bowler, and T. Miyazaki, J. Chem. Theory Comput. **10**, 4813 (2014).

[51] A. Nakata, D. R. Bowler, and T. Miyazaki, Phys. Chem. Chem. Phys. **17**, 31427 (2015).

[52] M. J. Rayson and P. R. Briddon, Phys. Rev. B **80**, 205104 (2009).

[53] M. J. Rayson, Comput. Phys. Commun. **181**, 1051 (2010).

[54] See Supplemental Material at http://link.aps.org/supplemental/10.1103/PhysRevB.102.144103 for additional structural details of the domain walls and supplementary electronic structure calculations.

[55] J. M. Soler, E. Artacho, J. D. Gale, A. García, J. Junquera, P. Ordejón, and D. Sánchez-Portal, J. Phys.: Condens. Matter **14**, 2745 (2002) .

[56] E. Artacho, D. Sánchez-Portal, P. Ordejón, A. García, and J. M. Soler, Phys. Status Solidi **215**, 809 (1999).

[57] P. E. Blöchl, Phys. Rev. B **50**, 17953 (1994).

[58] G. Kresse and J. Furthmüller, Phys. Rev. B **54**, 11169 (1996).

[59] G. Kresse and D. Joubert, Phys. Rev. B **59**, 1758 (1999).

[60] E. Bitzek, P. Koskinen, F. Gähler, M. Moseler, and P. Gumbsch, Phys. Rev. Lett. **97**, 170201 (2006).

[61] F. Birch, Phys. Rev. **71**, 809 (1947).

[62] N. A. Spaldin, J. Solid State Chem. **195**, 2 (2012).

[63] A. B. Mosberg, E. D. Roede, D. M. Evans, T. S. Holstad, E. Bourret, Z. Yan, A. T. J. Van Helvoort, and D. Meier, Appl. Phys. Lett. **115**, 122901 (2019).

[64] P. Schoenherr, K. Shapovalov, J. Schaab, Z. Yan, E. D. Bourret, M. Hentschel, M. Stengel, M. Fiebig, A. Cano, and D. Meier, Nano Lett. **19**, 1659 (2019).

[65] J. Schaab, K. Shapovalov, P. Schoenherr, J. Hackl, M. I. Khan, M. Hentschel, Z. Yan, E. Bourret, C. M. Schneider, S. Nemsák, M. Stengel, A. Cano, and D. Meier, Appl. Phys. Lett. **115**, 122903 (2019).

[66] T. S. Holstad, D. M. Evans, A. Ruff, D. R. Småbråten, J. Schaab, C. Tzschaschel, Z. Yan, E. Bourret, S. M. Selbach, S. Krohns, and D. Meier, Phys. Rev. B **97**, 085143 (2018).

[67] X. Wang, M. Mostovoy, M. G. Han, Y. Horibe, T. Aoki, Y. Zhu, and S. W. Cheong, Phys. Rev. Lett. **112**, 247601 (2014).

[68] A. Nakata, D. R. Bowler, and T. Miyazaki (unpublished).

[69] P. Marton, I. Rychetsky, and J. Hlinka, Phys. Rev. B **81**, 144125 (2010).

[70] K. C. Pitike, N. Khakpash, J. Mangeri, G. A. Rossetti, and S. M. Nakhmanson, J. Mater. Sci. **54**, 8381 (2019).

[71] P. Marton, A. Klíč, M. Paściak, and J. Hlinka, Phys. Rev. B **96**, 174110 (2017).

[72] H. L. Lin, K. L. Yang, P. Z. Chen, G. Z. Zhou, C. F. Li, S. H. Zheng, L. Lin, Z. B. Yan, X. P. Jiang, and J.-M. Liu, J. Appl. Phys. **127**, 194106 (2020).